A geometric analysis of slip rate variation with depth in listric normal faults

Yao Zhang*

College of Civil Engineering and Architecture, Zhejiang University of Water Resources and Electric Power, Hangzhou, China

Fault slip rates are critical parameters for assessing regional strain accumulation and seismic hazards. Previous investigations on fault slip rates primarily concentrated on shallow depths or along the strike of the fault, neglecting the variation with depth. This study focuses on listric normal faults, commonly observed in tectonic extensional zones, and investigates the variation of slip rates with depth. The relationships between slip rates along different fault segments are derived based on the inclined shear geometric models. The study finds that slip rates on different segments of listric normal faults are generally not equal and depend on the type of bend (concave or convex), the dip angles of the fault segments and axial surfaces. Inferring regional horizontal extension solely from shallow segment displacements or growth strata thickness may lead to inaccurate conclusions. In accordance with the methodology outlined in this paper, slip rates at various depths along the Chengnan Fault for the three time intervals: 24.6−33 Ma, 33−43.5 Ma, and 43.5−65 Ma, are estimated. The results of this study offer valuable insights into the kinematics of listric normal faults, facilitating a better comprehension of the discrepancy between slip rates measured at surface and slip rates measured at depth.

KEYWORDS

fault slip rate, listric normal fault, concave bend, convex bend, extensional rate

1 Introduction

The fault slip rate could be calculated by dividing the accumulated displacement by the timing of the displacement. Displacement is measured from geomorphic markers, trenching, gravity modeling and interpretation of seismic reflection data, whilst the timing of the displacement is determined by radiocarbon dating, tephrachronology, fission track dating and identification of fossils. The fault slip rate is a very important kinematic parameter of active faults, as it can be applied to evaluate regional strain accumulation and estimate seismic hazards (Anderson et al., 1996; Nicol et al., 1997; Galadini and Galli, 2000; Nicol et al., 2005; Nicol et al., 2006; Mouslopoulou et al., 2009; Blakeslee and Kattenhorn, 2013).

Listric normal faults are commonly observed in tectonic extensional zones. There have been numerous studies on fault slip rates of listric normal faults by previous researchers, revealing that fault slip rates vary with lateral position and time (Mitchell et al., 2001; Benedetti et al., 2002; Friedrich et al., 2003; Bull et al., 2006; Nicol et al., 2006; McClymont et al., 2009; Schlagenhauf et al., 2010; Schlagenhauf et al., 2011). Previous investigations indicate many listric normal faults show curvature in plan view, and slip rate is larger in the center along a fault trace than it is at the ends of a fault (Nicol et al., 2010; Zhang et al., 2020). However, how fault slip rates vary at different depths has been poorly studied. The variation of slip rate with depth in listric normal faults is an essential aspect to consider when studying
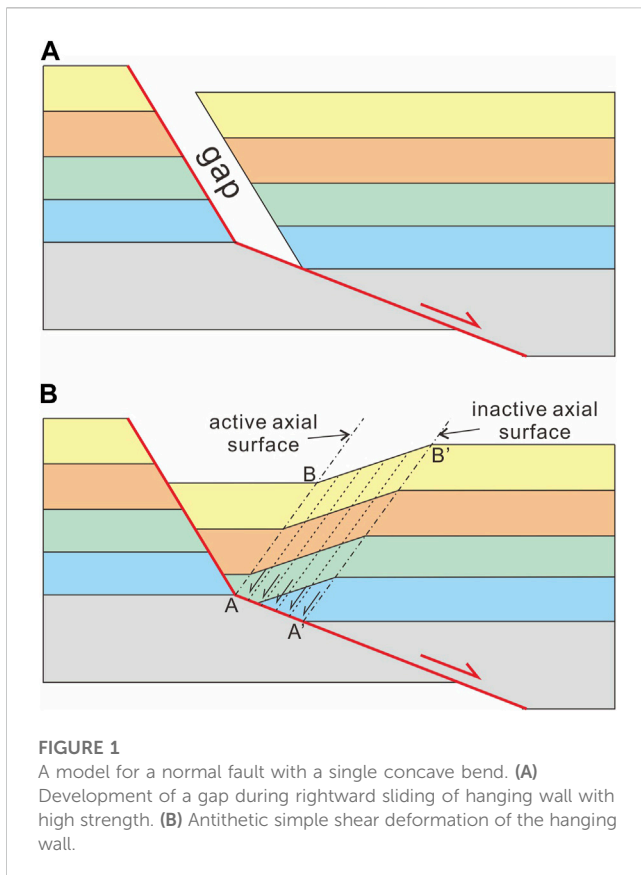
FIGURE 1
A model for a normal fault with a single concave bend. **(A)** Development of a gap during rightward sliding of hanging wall with high strength. **(B)** Antithetic simple shear deformation of the hanging wall.

FIGURE 2
A model for a normal fault with a single convex bend. **(A)** Overlap region development during rightward sliding of hanging wall with undeformed hanging wall. **(B)** Antithetic simple shear with reverse shear sense applied to the convex bend, contradicting the extensional characteristics of the deformation. **(C)** Synthetic simple shear with normal shear sense indicates a more plausible mechanism for the convex bend.

the mechanics of faulting and earthquake generation, as it influences the overall seismic behavior and deformation pattern within the fault zone. When using fault slip rates to estimate the average earthquake frequency, it is necessary to assume that surface measurements of slip rate represent slip rates at seismogenic depths (Youngs and Coppersmith, 1985). Understanding this variation is crucial for assessing seismic hazards and for developing accurate models of fault behavior in tectonically active regions. Therefore, the objective of this study is to investigate whether there are differences between surface fault slip rates and those at subsurface levels of listric normal faults based on geometric models, as well as to identify the factors controlling these differences.

2 Methods

The inclined shear model is employed to analyze the relationship between slip rates at different depths in listric normal faults, as this model is the predominant deformation mode for listric normal faults (Dula, 1991; Xiao and Suppe, 1992). Forward modeling and geometric analysis methods were extensively employed in this study. The following introduces the inclined shear model of listric normal faults.

Assuming the presence of a normal fault with a single concave bend, as the hanging wall moves, if the hanging wall has a significantly high strength, it will remain undeformed and a gap will develop between the hanging wall and the footwall (Figure 1A). However, in reality, the hanging wall does not possess sufficient
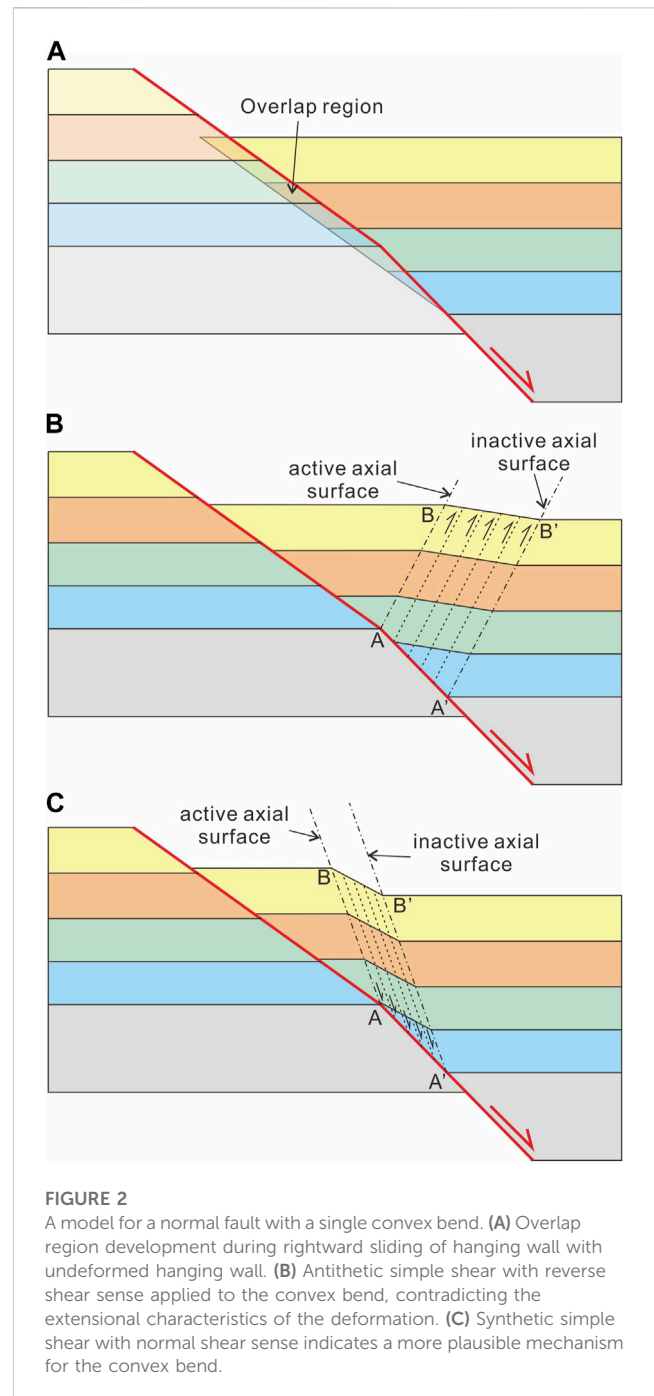
strength, resulting in its collapse and subsequent filling of the gap. Extensive research has demonstrated that antithetic normal faulting is a prevalent mechanism for the collapse deformation of the hanging wall (Figure 1B; White et al., 1986; Groshong, 1989; Dula, 1991; White and Yielding, 1991; Kerr and White, 1992; White, 1992; Xiao and Suppe, 1992; Withjack and Peterson, 1993; Withjack et al., 1995; Hauge and Gray, 1996; Withjack and Schlische, 2006). The collapse of the hanging wall of a fault induces tilting deformation of the strata, giving rise to a kink band comprising dipping beds. This kink band is delineated by two axial surfaces aligned in the direction of hanging wall collapse. Axial surface AB is located at the inflection point of the fault. Although it remains stationary relative to the
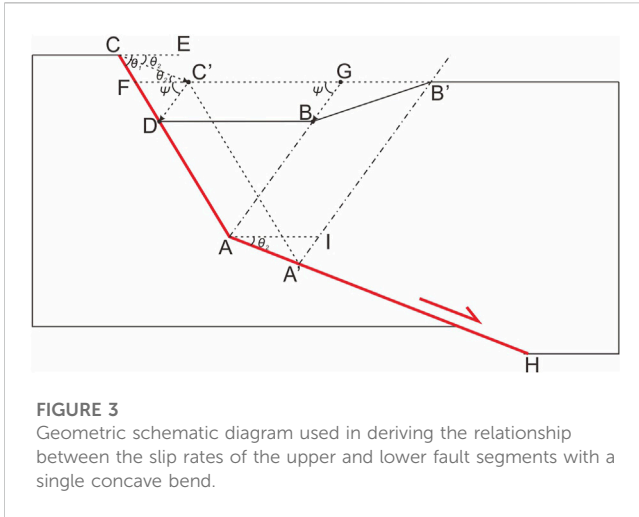
FIGURE 3
Geometric schematic diagram used in deriving the relationship between the slip rates of the upper and lower fault segments with a single concave bend.

FIGURE 4
Geometric schematic diagram used in deriving the relationship between the slip rates of the upper and lower fault segments with a single convex bend.
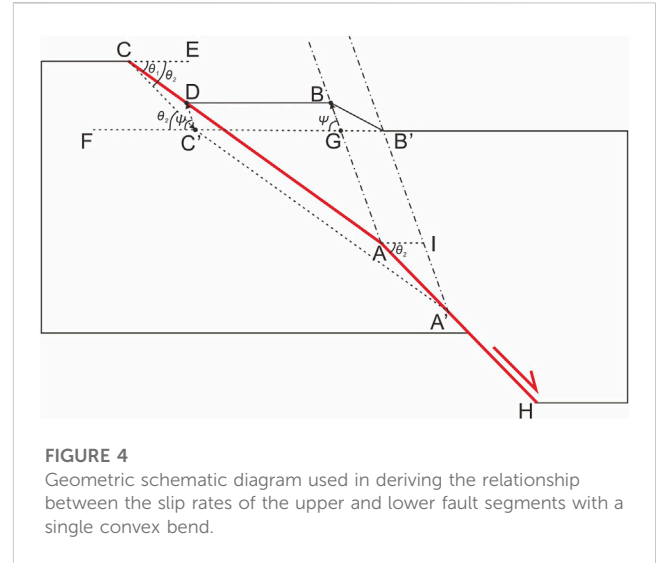
footwall and the fault, it is an active axial surface. This is because as the slip distance of the fault increases, the strata of the hanging wall pass through this surface and undergo tilting deformation. The initial position of axial surface $A'B'$ coincides with axial surface AB. As the fault slips, axial surface $A'B'$ moves along with the fault displacement. Axial surface $A'B'$ is an inactive axial surface because its position remains fixed relative to the hanging wall, and no new strata undergo deformation by passing through this surface when the fault slips.

Assuming the presence of a normal fault with a single convex bend, as the hanging wall moves, an overlap region will emerge between the hanging wall and the footwall if the former remains undeformed (Figure 2A). In order to prevent overlap, deformation of the hanging wall is necessary. However, if antithetic normal faulting is applied to convex bends, a reverse shear sense in the hanging wall would be required (Figure 2B), which contradicts the extensional characteristics of the deformation. Therefore, for convex bends, synthetic normal faulting represents a more plausible mechanism for the collapse deformation of the hanging wall (Figure 2C; Xiao and Suppe, 1992).

3 Results

3.1 Fault slip rates calculation with one fault bend

3.1.1 Concave fault bend

Consider the simple case of one concave fault bend, as shown in Figure 3. The angle $\angle ECD$, representing the dip of the upper fault segment, is equal to θ_1. The angle $\angle HAI$, representing the dip of the lower fault segment, is equal to θ_2. The angle $\angle FGB$, representing the dip of the axial surface, is equal to ψ.

If the hanging wall undergoes a displacement AA' along the lower fault segment, the position of point C will be relocated to point C'. Thus, we have

$$CC' \parallel AA' \, and \, CC' = AA' \tag{1}$$

$$\therefore \angle EEC' = \angle FC'C = \angle HAI = \theta_2 \tag{2}$$

$$\therefore \angle DCC' = \angle ECD - \angle ECC' = \theta_1 - \theta_2 \tag{3}$$

Throughout the deformation of the hanging wall, the displacement of point C' results in its relocation to point D, while the displacement of point G leads to its relocation to point B. Thus, we have

$$C'D \parallel GB \tag{4}$$

$$\therefore \angle FC'D = \angle FGB = \psi \tag{5}$$

$$\therefore \angle CC'D = \angle FC'D + \angle FC'C = \psi + \theta_2 \tag{6}$$

Applying the law of sines to $\Delta CDC'$, we have

$$\frac{CD}{\sin \angle CC'D} = \frac{CC'}{\sin \angle CDC'} = \frac{AA'}{\sin \left(\angle DCC' + \angle CC'D \right)} \tag{7}$$

$$\therefore \sin \left(\psi + \theta_1 \right) \cdot CD = \sin \left(\psi + \theta_2 \right) \cdot AA' \tag{8}$$

If we only know the displacement of slip along the upper segment of the fault CD. Given the knowledge of the duration of fault slip, we obtain

$$r_1 = \frac{CD}{t} \tag{9}$$

where r_1 is the slip rate along the upper segment, t is the duration of fault slip.

Combining Eqs 8, 9, we obtain

$$r_2 = \frac{AA'}{t} = \frac{\sin \left(\psi + \theta_1 \right)}{\sin \left(\psi + \theta_2 \right)} \cdot \frac{CD}{t} = \frac{\sin \left(\psi + \theta_1 \right)}{\sin \left(\psi + \theta_2 \right)} r_1 \tag{10}$$

where r_2 is the slip rate along the lower segment.

3.1.2 Convex fault bend

Consider the simple case of one convex fault bend, as shown in Figure 4. The angle $\angle ECD$, representing the dip of the upper fault segment, is equal to θ_1. The angle $\angle HAI$, representing the dip of the lower fault segment, is equal to θ_2. The angle $\angle FGB$, representing the dip of the axial surface, is equal to ψ.

If the hanging wall undergoes a displacement AA' along the lower fault segment, the position of point C will be relocated to point C'. Thus, we have
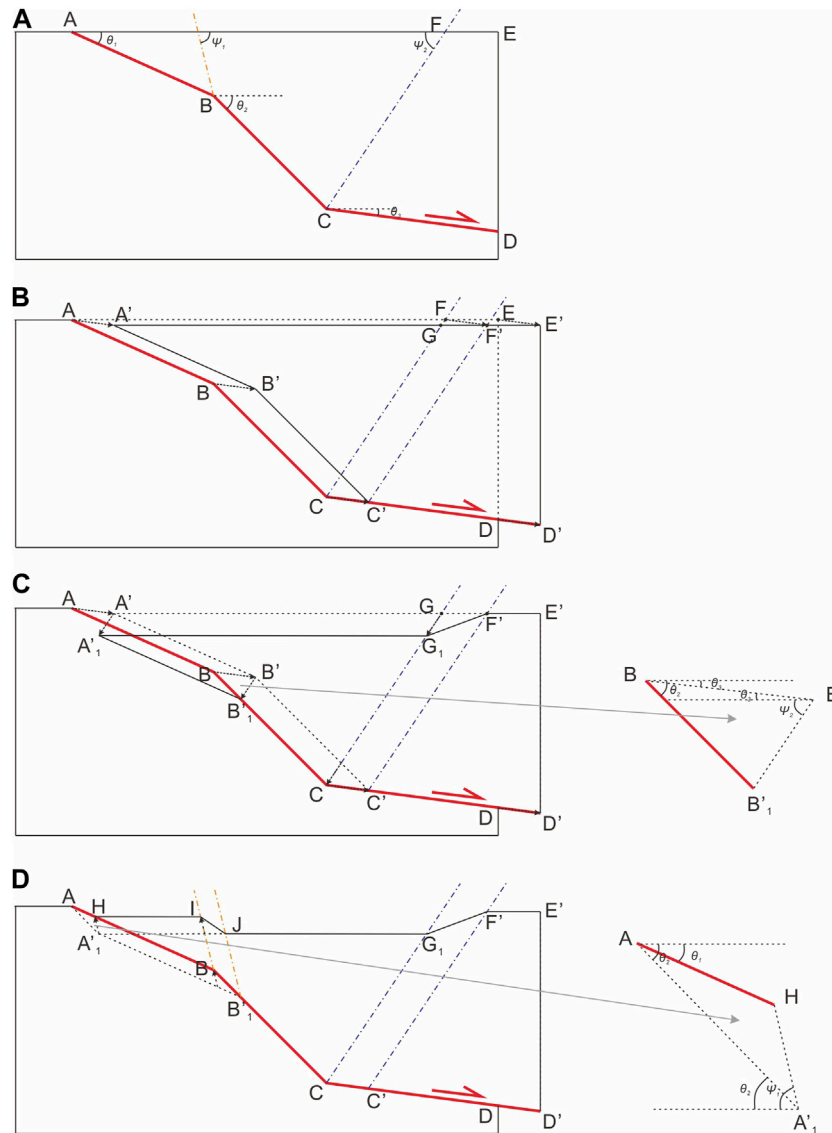
FIGURE 5
Geometric schematic diagram used in deriving the relationship between the slip rates of different fault segments with multiple fault bends. **(A)** Initial state of a fault with a concave bend and a convex bend. **(B)** The hanging wall slips along the lower fault segment with a displacement of CC' during the first stage. **(C)** The polygon A'B'C'F' of the hanging wall deforms to form the polygon A1'B1'CC'F'G1 during the second stage. **(D)** The polygon A1'B1'CC'F'G1 deforms to form the polygon HBCC'F'G1JI during the final stage.

$$CC' \parallel AA' \, and \, CC' = AA' \tag{11}$$

$$\therefore \angle EEC' = \angle FC'C = \angle HAI = \theta_2 \tag{12}$$

$$\therefore \angle DCC' = \angle ECC' - \angle ECD = \theta_2 - \theta_1 \tag{13}$$

Throughout the deformation of the hanging wall, the displacement of point C' results in its relocation to point D, while the displacement of point G leads to its relocation to point B. Thus, we have

$$C'D \parallel GB \tag{14}$$

$$\therefore \angle FC'D = \angle FGB = \psi \tag{15}$$

$$\therefore \angle CC'D = \angle FC'D - \angle FC'C = \psi - \theta_2 \tag{16}$$

Applying the law of sines to $\triangle CDC'$, we have

$$\frac{CD}{\sin \angle CC'D} = \frac{CC'}{\sin \angle CDC'} = \frac{AA'}{\sin (\angle DCC' + \angle CC'D)} \tag{17}$$

$$\sin (\psi - \theta_1) \cdot CD = \sin (\psi - \theta_2) \cdot AA' \tag{18}$$

In the majority of cases, we only know the displacement of slip along the upper segment of the fault CD. Given the knowledge of the duration of fault slip, we obtain

$$r_1 = \frac{CD}{t} \tag{19}$$

where r_1 is the slip rate along the upper segment, t is the duration of fault slip.

Combining Eqs 18, 19, we obtain

$$r_2 = \frac{AA'}{t} = \frac{\sin(\psi - \theta_1)}{\sin(\psi - \theta_2)} \cdot \frac{CD}{t} = \frac{\sin(\psi - \theta_1)}{\sin(\psi - \theta_2)} r_1 \qquad (20)$$

where r_2 is the slip rate along the lower segment.

3.2 Fault slip rates calculation with multiple fault bends

Now that we have established the slip rate law for a fault with a single fault bend, we shall proceed to investigate the slip rate law for faults with multiple fault bends. In the case of continuously curved listric normal faults, we can treat them as a large number of fault bends between arbitrarily small, straight, fault segments.

Consider a fault with one concave fault bend and one convex fault bend, as depicted in Figure 5A. The dip of the upper fault segment is θ_1. The dip of the middle fault segment is θ_2. The dip of the lower fault segment is θ_3. The dip of the synthetic upper axial surface is ψ_1. The dip of the antithetic lower axial surface is ψ_2.

For the convenience of calculation, we partition the deformation into three steps.

Firstly, the hanging wall undergoes displacement CC' along the lower fault segment. Consequently, points A, B, C, D, E, and F move to points A', B', C', D', E', and F', respectively (Figure 5B). Thus, we have

$$\overrightarrow{AA'} = \overrightarrow{BB'} = \overrightarrow{CC'} \qquad (21)$$

Secondly, the collapse deformation of the polygon A'B'C'F' of the hanging wall forms the polygon A1'B1'CC'F'G1 (Figure 5C). Applying the law of sines to $\Delta BB'B'1$, we have

$$\frac{BB'_1}{\sin \angle BB'B'_1} = \frac{BB'}{\sin \angle B'_1B'} = \frac{CC'}{\sin(\angle B'_1BB' + \angle B'_1B'B)} \qquad (22)$$

$$\therefore \sin(\psi_2 + \theta_2) \cdot BB'_1 = \sin(\psi_2 + \theta_3) \cdot CC' \qquad (23)$$

Finally, the polygon A1'B1'CC'F'G1 undergoes deformation to form the polygon HBCC'F'G1JI (Figure 5D). Applying the law of sines to $\Delta AHA'1$, we have

$$\frac{AH}{\sin \angle AA'_1H} = \frac{AA'_1}{\sin \angle AHA'_1} = \frac{BB'_1}{\sin(\angle HAA'_1 + \angle HA'_1A)} \qquad (24)$$

$$\therefore \sin(\psi_1 - \theta_1) \cdot AH = \sin(\psi_1 - \theta_2) \cdot BB'_1 \qquad (25)$$

Based on the aforementioned analysis, it can be readily inferred that the displacement relationship on both sides of a fault bend is solely determined by the type of bend (concave or convex), the individual dip angles of the respective fault segments, and the dip angle of the axial surface at the bend, independent of other factors.

Therefore, for a fault with n segments and n-1 bends, the following relationships hold:

$$if \; i-th \, bend \, is \, concave: \; \sin(\psi_i + \theta_i) \cdot x_i = \sin(\psi_i + \theta_{i+1}) \cdot x_{i+1} \qquad (26)$$

$$if \; i-th \, bend \, is \, convex: \; \sin(\psi_i - \theta_i) \cdot x_i = \sin(\psi_i - \theta_{i+1}) \cdot x_{i+1} \qquad (27)$$

where θ_i represents the dip angle of the i-th fault segment, θ_{i+1} represents the dip angle of the (i+1)-th fault segment, ψ_i is the dip
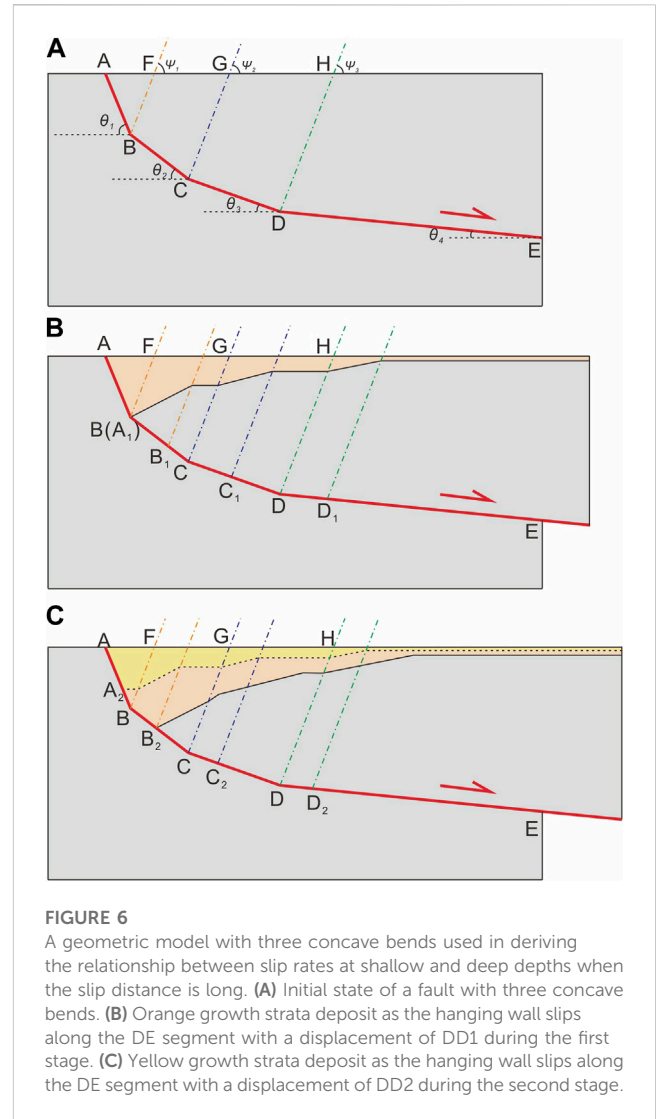

FIGURE 6
A geometric model with three concave bends used in deriving the relationship between slip rates at shallow and deep depths when the slip distance is long. **(A)** Initial state of a fault with three concave bends. **(B)** Orange growth strata deposit as the hanging wall slips along the DE segment with a displacement of DD1 during the first stage. **(C)** Yellow growth strata deposit as the hanging wall slips along the DE segment with a displacement of DD2 during the second stage.

angle of the i-th axial surface, x_i is the displacement on the i-th fault segment, x_{i+1} is the displacement on the (i + 1)-th fault segment.

Based on Eqs 26, 27, if the dip angles of each fault segment, the properties of each fault bend, the dip angles of each axial surface, and the displacement on one of the fault segments are known, then the displacements on the remaining fault segments can be derived. Furthermore, if the duration of motion is also known, the slip rates on each segment can be obtained.

It is noteworthy that if each bend in the fault is either convex or concave in shape, and the dip angles of the axial surfaces are identical, the following relationships hold:

$$if \, all \, the \, bend \, are \, concave: \; \sin(\psi + \theta_i) \cdot x_i = \sin(\psi + \theta_j) \cdot x_j \qquad (28)$$

$$if \, all \, the \, bend \, are \, concex: \; \sin(\psi - \theta_i) \cdot x_i = \sin(\psi - \theta_j) \cdot x_j \qquad (29)$$

where θ_i represents the dip angle of the i-th fault segment, θ_j represents the dip angle of the j-th fault segment, ψ is the dip angle of the axial surface, x_i is the displacement on the i-th fault segment, x_j is the displacement on the j-th fault segment.

Eqs 28, 29 indicate that if the dip angle of the axial surface and the displacement on one of the fault segments are known, determining the displacement on another fault segment only requires knowledge of its corresponding dip angle. This implies that once the dip angles of two fault segments are determined, regardless of the number of intervening fault segments or their dip angles, it will not alter the relationship between the displacements of these two fault segments.

This conclusion is highly useful because in most cases, bends of listric normal faults tend to be concave in shape. If the mechanical properties of the hanging wall are similar, the dip angle of the axial surface remains relatively constant. So even if we only have access to fault displacements and rates at the surface or shallow depths, we can infer the displacements and slip rates along the deeper fault segments. Furthermore, the horizontal extension rate can be inferred since listric normal faults tend to flatten at depth:

$$r_e = r_d = \frac{\sin(\psi + \theta_s)}{\sin(\psi + \theta_d)} r_s \qquad (30)$$

where θ_s represents the dip angle of the shallow segment of the fault, θ_d represents the dip angle of the deepest horizontal segment of the fault, ψ is the dip angle of the axial surface, r_e is the horizontal extension rate, r_d is the slip rate along the deepest horizontal segment of the fault. r_s is the slip rate along the shallow segment of the fault.

3.3 Long slip distance of faults

Previously, we only discussed the case where the slip distance was limited to a small segment of the fault. Now, we will analyze the scenario where the slip distance is longer and spans across multiple fault segments.

Consider a fault with three concave fault bends, as depicted in Figure 6A. The dip of the fault segment AB is θ_1. The dip of the fault segment BC is θ_2. The dip of the fault segment CD is θ_3. The dip of the fault segment DE is θ_4. The dip of the axial surface BF is ψ_1. The dip of the axial surface CG is ψ_2. The dip of the axial surface DH is ψ_3.

If Figure 6C represents the final state after deformation, the deformation process can be divided into two stages. During the first stage, the hanging wall slides a distance of DD1 along the DE segment. At this point, the sliding distance along the AB segment is AA1 (Figure 6B). Based on the Eqs 26, 27, we have

$$\sin(\psi_1 + \theta_1) \cdot AB = \sin(\psi_1 + \theta_2) \cdot BB_1 \qquad (31)$$
$$\sin(\psi_2 + \theta_2) \cdot BB_1 = \sin(\psi_2 + \theta_3) \cdot CC_1 \qquad (32)$$
$$\sin(\psi_3 + \theta_3) \cdot CC_1 = \sin(\psi_3 + \theta_4) \cdot DD_1 \qquad (33)$$

Combining Eqs 31–33, we obtain the relationship between AB and DD1:

$$DD_1 = \frac{\sin(\psi_1 + \theta_1) \cdot \sin(\psi_2 + \theta_2) \cdot \sin(\psi_3 + \theta_3)}{\sin(\psi_1 + \theta_2) \cdot \sin(\psi_2 + \theta_3) \cdot \sin(\psi_3 + \theta_4)} \cdot AB \qquad (34)$$

Subsequently, the hanging wall slides a distance of DD2 along the DE segment, while the sliding distance along the AB segment is AA2 (Figure 6C). Based on the Eqs 26, 27, we have

$$\sin(\psi_1 + \theta_1) \cdot AA_2 = \sin(\psi_1 + \theta_2) \cdot BB_2 \qquad (35)$$
$$\sin(\psi_2 + \theta_2) \cdot BB_2 = \sin(\psi_2 + \theta_3) \cdot CC_2 \qquad (36)$$
$$\sin(\psi_3 + \theta_3) \cdot CC_2 = \sin(\psi_3 + \theta_4) \cdot DD_2 \qquad (37)$$

Combining (Eqs 36, 37), we obtain the relationship between BB2 and DD2:

$$DD_2 = \frac{\sin(\psi_2 + \theta_2) \cdot \sin(\psi_3 + \theta_3)}{\sin(\psi_2 + \theta_3) \cdot \sin(\psi_3 + \theta_4)} \cdot BB_2 \qquad (38)$$

If we know the lengths of AB and BB1 in the final state, as well as the duration of time elapsed from the initial state to the final state, we can obtain the fault slip rate along the DE segment during this time period by utilizing (Eqs 34, 38):

$$
\begin{aligned}
r_{DE} &= \frac{DD_1 + DD_2}{t} \\
&= \frac{\sin(\psi_1 + \theta_1) \cdot \sin(\psi_2 + \theta_2) \cdot \sin(\psi_3 + \theta_3)}{\sin(\psi_1 + \theta_2) \cdot \sin(\psi_2 + \theta_3) \cdot \sin(\psi_3 + \theta_4)} \cdot \frac{AB}{t} \\
&+ \frac{\sin(\psi_2 + \theta_2) \cdot \sin(\psi_3 + \theta_3)}{\sin(\psi_2 + \theta_3) \cdot \sin(\psi_3 + \theta_4)} \cdot \frac{BB_2}{t}
\end{aligned}
\qquad (39)
$$

where r_{DE} represents the fault slip rate along the DE segment, t represents the duration of time elapsed from the initial state to the final state.

If the dip angles of axial surfaces are equal to ψ, then Equation 39 can be simplified to

$$r_{DE} = \frac{DD_1 + DD_2}{t} = \frac{\sin(\psi + \theta_1)}{\sin(\psi + \theta_4)} \cdot \frac{AB}{t} + \frac{\sin(\psi + \theta_2)}{\sin(\psi + \theta_4)} \cdot \frac{BB_2}{t} \qquad (40)$$

If orange and yellow growth strata were sequentially deposited during the first and second stages of fault slip, it may be feasible to deduce the duration of each stage (Figure 6C). This information can be used to determine the slip rate of the fault along segment DE for each stage period:

$$
\begin{aligned}
r_{DE1} &= \frac{\sin(\psi_1 + \theta_1) \cdot \sin(\psi_2 + \theta_2) \cdot \sin(\psi_3 + \theta_3)}{\sin(\psi_1 + \theta_2) \cdot \sin(\psi_2 + \theta_3) \cdot \sin(\psi_3 + \theta_4)} \cdot \frac{A_2B}{t_1} \\
&+ \frac{\sin(\psi_2 + \theta_2) \cdot \sin(\psi_3 + \theta_3)}{\sin(\psi_2 + \theta_3) \cdot \sin(\psi_3 + \theta_4)} \cdot \frac{BB_2}{t_1}
\end{aligned}
\qquad (41)
$$

$$r_{DE2} = \frac{\sin(\psi_1 + \theta_1) \cdot \sin(\psi_2 + \theta_2) \cdot \sin(\psi_3 + \theta_3)}{\sin(\psi_1 + \theta_2) \cdot \sin(\psi_2 + \theta_3) \cdot \sin(\psi_3 + \theta_4)} \cdot \frac{AA_2}{t_2} \qquad (42)$$

where r_{DE1} represents the fault slip rate along the DE segment during the deposition of the orange growth strata in the first stage, r_{DE2} represents the fault slip rate along the DE segment during the deposition of the yellow growth strata in the second stage, t_1 represents the duration of the deposition of the orange growth strata during the first stage. t_2 represents the duration of the deposition of the yellow growth strata during the second stage.

If the dip angles of axial surfaces are equal to ψ, then Eqs 41, 42 can be simplified to

$$r_{DE1} = \frac{\sin(\psi + \theta_1)}{\sin(\psi + \theta_4)} \cdot \frac{A_2B}{t_1} + \frac{\sin(\psi + \theta_2)}{\sin(\psi + \theta_4)} \cdot \frac{BB_2}{t_1} \qquad (43)$$

$$r_{DE2} = \frac{\sin(\psi + \theta_1)}{\sin(\psi + \theta_4)} \cdot \frac{AA_2}{t_2} \qquad (44)$$
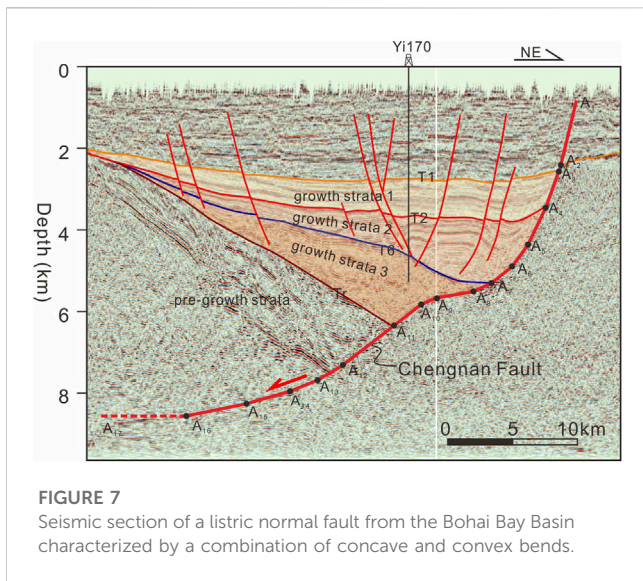
FIGURE 7
Seismic section of a listric normal fault from the Bohai Bay Basin characterized by a combination of concave and convex bends.

TABLE 1 Dip angles and lengths of each fault segment.

Fault segments	Dip angles (°)	Lengths (m)
A_1A_2	52.56	-
A_2A_3	52.56	-
A_3A_4	41.45	1329
A_4A_5	33.50	1657
A_5A_6	23.10	1348
A_6A_7	14.17	1656
A_7A_8	8.26	1414
A_8A_9	3.09	2847
A_9A_{10}	7.99	1180
$A_{10}A_{11}$	13.95	2211
$A_{11}A_{12}$	13.78	-
$A_{12}A_{13}$	10.59	-
$A_{13}A_{14}$	7.18	-
$A_{14}A_{15}$	5.13	-
$A_{15}A_{16}$	3.69	-
$A_{16}A_{17}$	0.00	-

TABLE 2 Conversion of lengths of segments A3A4 to A10A11 into lengths at different dip angles (m).

Fault segments	52.56° (A_2A_3)	41.45° (A_3A_4)	33.50° (A_4A_5)	23.10° (A_5A_6)	14.17° (A_6A_7)	8.26° (A_7A_8)	3.09° (A_8A_9)	7.99° (A_9A_{10})	13.95° ($A_{10}A_{11}$)	13.78° ($A_{11}A_{12}$)	10.59° ($A_{12}A_{13}$)	7.18° ($A_{13}A_{14}$)	5.13° ($A_{14}A_{15}$)	3.69° ($A_{15}A_{16}$)	0.00° ($A_{16}A_{17}$)
A_3A_4	1410	1329	1305	1312	1354	1402	1461	1553	1700	1701	1732	1772	1801	1822	1886
A_4A_5	1791	1688	1657	1666	1720	1781	1855	1972	2159	2161	2200	2251	2287	2315	2396
A_5A_6	1449	1365	1340	1348	1391	1440	1500	1595	1746	1748	1779	1820	1849	1872	1938
A_6A_7	1726	1626	1597	1605	1656	1716	1787	1900	2080	2082	2119	2168	2203	2230	2308
A_7A_8	1422	1340	1316	1323	1365	1414	1473	1566	1715	1716	1747	1788	1816	1838	1903
A_8A_9	2749	2590	2543	2557	2639	2733	2847	3026	3313	3316	3376	3454	3509	3552	3677
A_9A_{10}	1072	1010	991	997	1029	1065	1110	1180	1292	1293	1316	1347	1368	1385	1433

4 Geological example

A seismic section from the Bohai Bay Basin is presented as an illustrative example of how slip rates at various depths during different time intervals are calculated (Figure 7). In the seismic section, the Chengnan Fault is identified as a listric normal fault characterized by a combination of concave and convex bends. During the Paleogene period, the Bohai Bay Basin underwent substantial extensional tectonics, leading to pronounced activity along the Chengnan Fault within this geological epoch (Qi and Yang, 2010; Li et al., 2012; Zhao et al., 2016). Three sequences of

TABLE 3 Slip rates of the Chengnan fault at various segments during three time intervals: 24.6–33 Ma, 33–43.5 Ma, and 43.5–65 Ma (m/Ma).

Time intervals	Segment A₂A₃	Segment A₃A₄	Segment A₄A₅	Segment A₅A₆	Segment A₆A₇	Segment A₇A₈	Segment A₈A₉	Segment A₉A₁₀	Segment A₁₀A₁₁	Segment A₁₁A₁₂	Segment A₁₂A₁₃	Segment A₁₃A₁₄	Segment A₁₄A₁₅	Segment A₁₅A₁₆	Segment A₁₆A₁₇
24.6–33 Ma	168	158	155	156	161	167	174	185	202	203	206	211	214	217	225
33–43.5 Ma	473	446	438	440	454	470	490	521	570	570	581	594	604	611	633
43.5–65 Ma	329	310	305	306	316	327	341	362	397	397	404	414	420	425	440

growth strata (Growth Strata 1, Growth Strata 2, Growth Strata 3) were deposited on the hanging wall of the fault, each delimited by reflection boundaries T1, T2, T6, and Tr. The corresponding ages for these reflection boundaries are 24.6 Ma, 33 Ma, 43.5 Ma, and 65 Ma, respectively (Ren, 2004; Yao et al., 2007a; Yao et al., 2007b). Growth strata 1 is constrained by seismic reflection boundaries T1 and T2, indicating sedimentation occurred between 24.6 Ma and 33 Ma. Growth strata 2 is defined by seismic reflection boundaries T2 and T6, suggesting sedimentation took place between 33 Ma and 43.5 Ma. Lastly, Growth strata 3 is delimited by seismic reflection boundaries T6 and Tr, indicating sedimentation occurred between 43.5 Ma and 65 Ma. In the following, the calculation of slip rates for the Chengnan Fault at various depths during the intervals of 24.6–33 Ma, 33–43.5 Ma, and 43.5–65 Ma are estimated.

Initially, it is necessary to replace the curved Chengnan Fault with multiple straight segments (from A1A2 to A16A17) and measure the dip angle of each segment (Table 1). It is worth noting that to calculate the true dip angle of the fault, it is necessary to adjust the lateral and vertical scales of the seismic profile to be consistent.

Subsequently, the lengths of the fault segments involved in the growth strata (from A3A4 to A10A11) are measured (Table 1). Utilizing Eqs 26, 27 to convert the lengths of segments from A3A4 to A10A11 into lengths at different dip angles (Table 2). For example, the length of segment A3A4 is 1329 m, with a dip angle of 41.45°. When converted to a dip angle of 52.56°, which is the angle for segment A2A3, the length becomes 1410 m.

Finally, sum the results of the converted segments involved in different time intervals and divide by the time intervals to obtain the slip rates of the Chengnan Fault at different fault segments, or different depths, during different time periods. For instance, during the deposition of Growth Strata 2, which corresponds to the time interval of 33–43.5 Ma, the fault segments involved are A4A5, A5A6, and A6A7. To determine the slip rate of the fault at segment A2A3 during the 33–43.5 Ma period, the lengths of A4A5, A5A6, and A6A7 are converted to a 52.56° dip angle, resulting in lengths of 1791 m, 1449 m, and 1726 m, respectively. These lengths are then summed to obtain 4966 m and divided by the time interval of 10.5 Ma, resulting in a calculated slip rate of 473 m/Ma. The slip rate results for each fault segment within the three time intervals: 24.6–33 Ma, 33–43.5 Ma, and 43.5–65 Ma, are presented in Table 3; Figure 8.

From Figure 8, it can be observed that the fault slip rate along the Chengnan Fault decreases gradually from segment A2A3 to A4A5. However, from segment A4A5 onwards and all the way to segment A16A17, the slip rate gradually increases. The maximum slip rate occurs at segment A16A17, while the minimum is observed at segment A4A5, resulting in a ratio of 1.45 between the two. The following discussion section will analyze the patterns of slip rate variations along different segments.

5 Discussion

5.1 Concave fault bend

For a fault with only one concave fault bend, the relationship between the slip rates along the upper segment and the lower segment can be determined based on Equation 10:
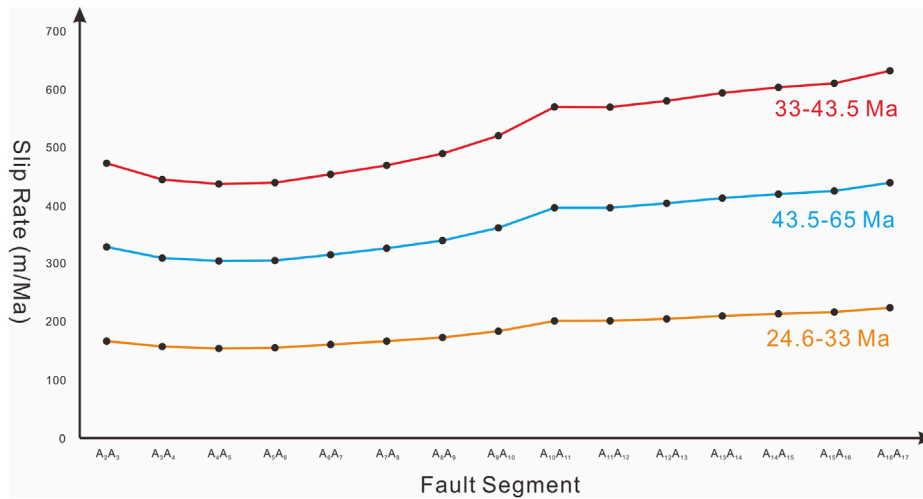
FIGURE 8
Line plot of fault slip rates along segments of the Chengnan Fault during the periods 24.6–33 Ma, 33–43.5 Ma, and 43.5–65 Ma.
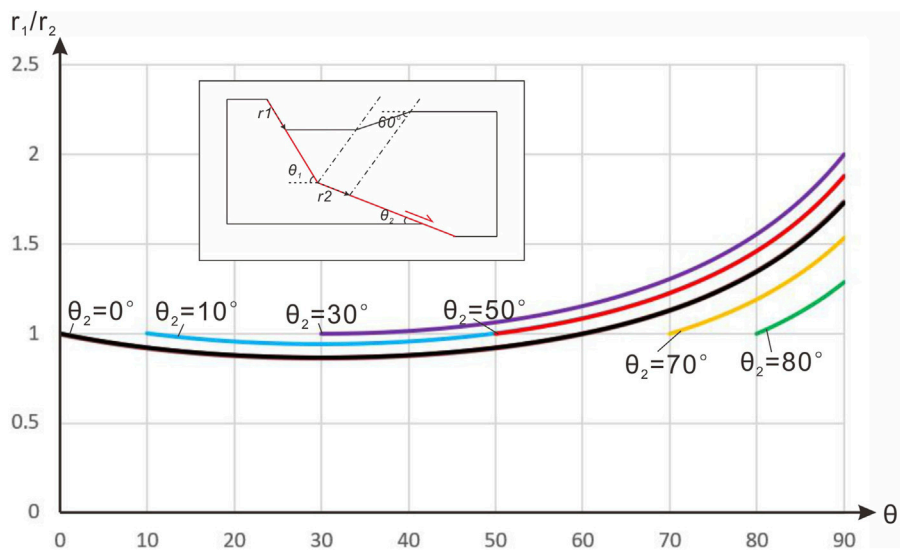

FIGURE 9
Graph of relationships between the value of r_1/r_2, the dip of the upper fault segment θ_1 and the dip of the lower fault segment θ_2 for a normal fault with a single concave bend.

$$\frac{r_1}{r_2} = \frac{\sin(\psi + \theta_2)}{\sin(\psi + \theta_1)} \qquad (45)$$

where r_1 is the slip rate along the upper fault segment, r_2 is the slip rate along the lower segment, ψ is the dip angle of axial surface, θ_1 representing the dip of the upper fault segment, θ_2 representing the dip of the lower fault segment.

Previous studies have suggested that the angle ψ is approximately around 60° ± 10° (Xiao and Suppe, 1992; Hauge and Gray, 1996). Here, we take ψ as 60° as an example to investigate the proportional relationship between r_1 and r_2 under different values of θ_1 and θ_2.

Figure 9 depicts the values of r_1/r_2 corresponding to different θ_1 when θ_2 is respectively set at 0°, 10°, 30°, 50°, 70°, and 80°. Based on the results, θ_2 can be divided into two cases. In the first case, when θ_2 ranges from 0° to 30°, the r_1/r_2 values initially decrease with increasing θ_1, reaching a minimum value at $\theta_1 = 30°$. Subsequently, the r_1/r_2 values increase with increasing θ_1, and the magnitude of the increase is greater than the decrease. In the second case, when θ_2 ranges from 30° to 90°, the r_1/r_2 values consistently increase with increasing θ_1. Furthermore, the result reveals that the minimum value of r_1/r_2 occurs at $\theta_1 = 30°$ and $\theta_2 = 0°$, approximately 0.866, while the maximum value of r_1/r_2 occurs at $\theta_1 = 90°$ and $\theta_2 = 30°$, equaling 2.
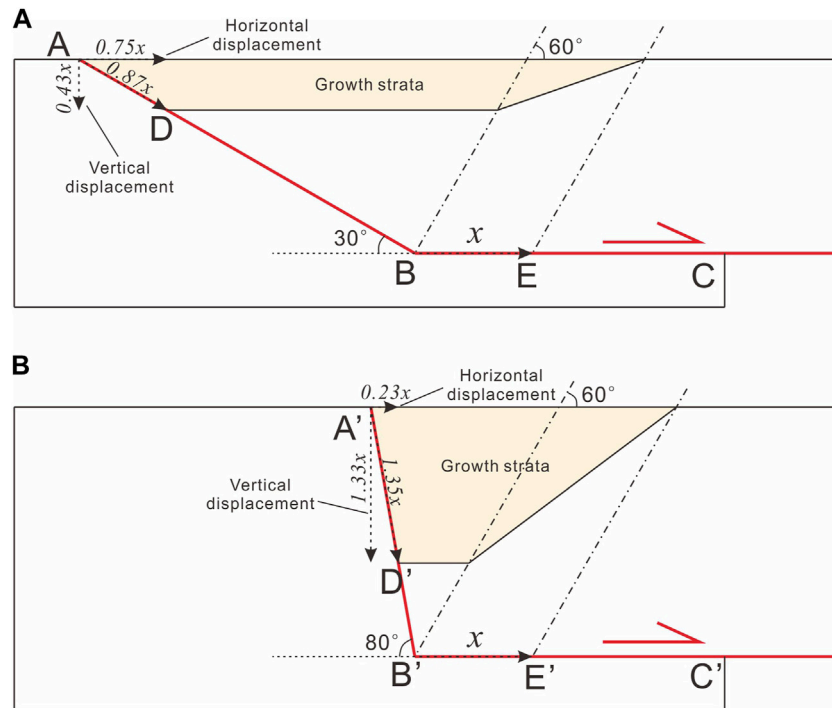
FIGURE 10
Comparative diagram of concave normal faults with equal extensional rates but varied dip angles of upper segment. **(A)** A concave normal fault model with 30° dip of upper segment. **(B)** A concave normal fault model with 80° dip of upper segment.
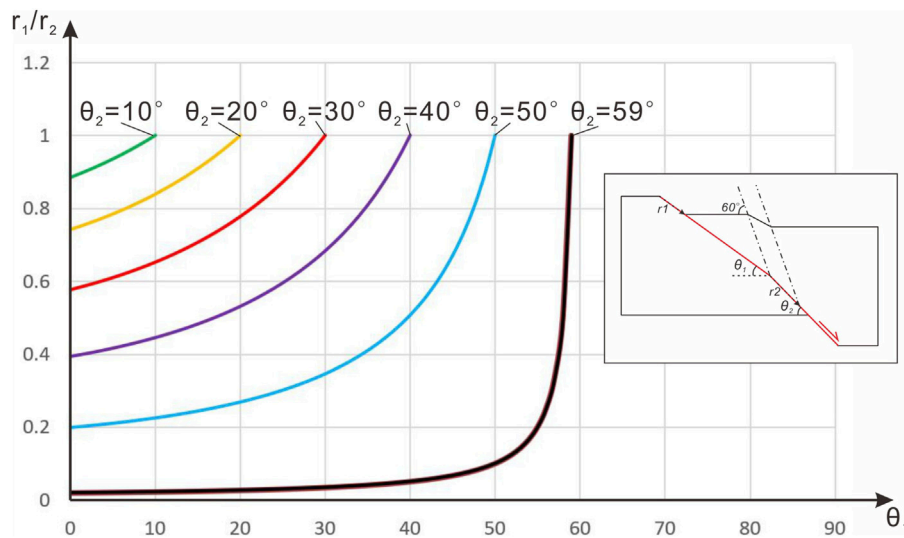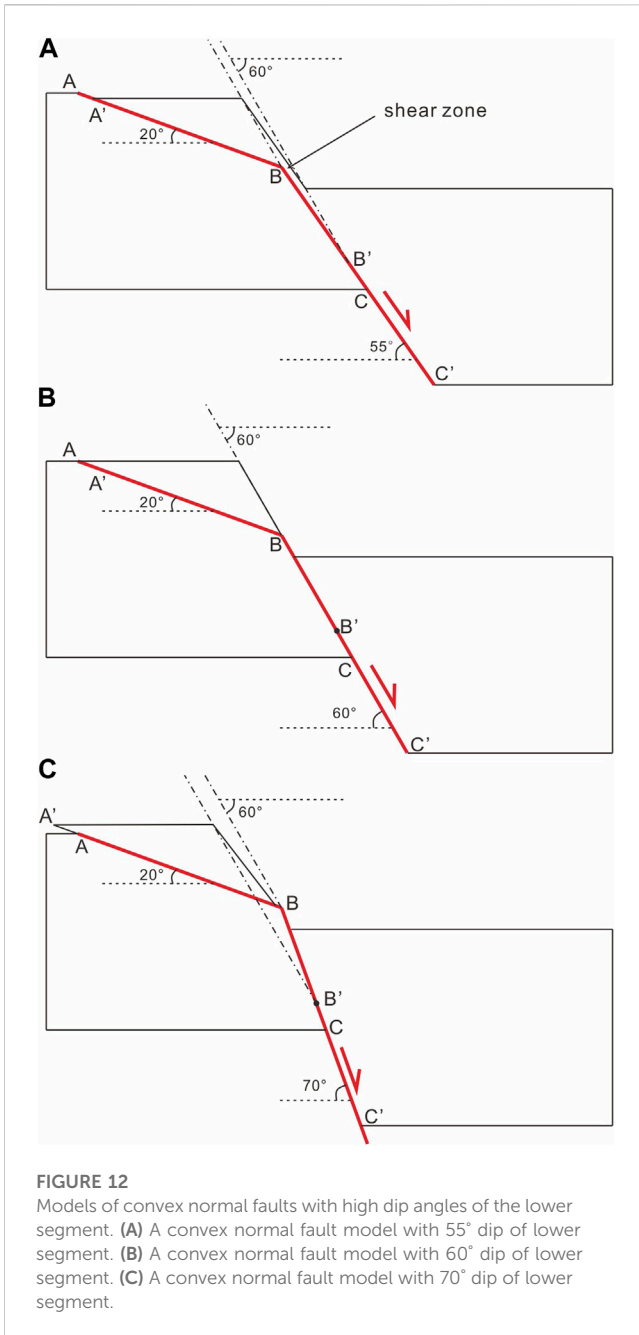

FIGURE 11
Graph of relationships between the value of r_1/r_2, the dip of the upper fault segment θ_1 and the dip of the lower fault segment θ_2 for a normal fault with a single convex bend.

Furthermore, it can be observed that as the value of θ_2 decreases, the probability of r_1/r_2 being less than 1 increases. For instance, when θ_2 is set to 0°, r_1/r_2 values are less than 1 for θ_1 ranging from 0° to 60°. Similarly, when θ_2 is 10°, r_1/r_2 values are less than 1 for θ_1 ranging from 10° to 50°. Additionally, it can be noted that when θ_2 exceeds 30°, regardless of the value of θ_1, r_1/r_2 values are greater than

1. Similarly, when θ_1 exceeds 60°, regardless of the value of θ_2, r_1/r_2 values are greater than 1.

The above analysis reveals that, in most cases, the slip rates on different segments of a listric normal fault are not equal. If the surface or shallow segments of the listric normal fault exhibit a large dip angle, the slip rate along these segments is often greater than that

FIGURE 12
Models of convex normal faults with high dip angles of the lower segment. **(A)** A convex normal fault model with 55° dip of lower segment. **(B)** A convex normal fault model with 60° dip of lower segment. **(C)** A convex normal fault model with 70° dip of lower segment.

of the deeper segments, with a maximum ratio of two times. For the listric normal fault, as it tends to be nearly horizontal at greater depths, the slip rate obtained on the shallow fault segment with a large dip angle is generally larger than that at deeper depths, potentially up to twice as large. It should be noted that listric normal faults may also exhibit flexure at the kilometer scale due to the rheology of the crust. However, due to the limited variation in dip angles, the impact on fault slip rates can be considered negligible according to Eq. 45.

Conversely, if the surface or shallow segments of the listric normal fault have a small dip angle, the slip rate along these segments tends to be smaller than that of the deeper segments, but the difference between the two is relatively close. In the latter case, the minimum ratio is approximately 0.866 times that of the deeper segments.

Another noteworthy observation is that for two faults with the same dip angle in the deep segment, even if their actual slip distances at depth are equal, significant differences in the displacement exhibited in the shallow segment can arise if the dip angles of the shallow segments are different.

For instance, consider fault ABC and fault A′B′C′, where the dip angles of segments BC and B′C′ are both 0°, the dip angle of segment AB is 30°, and the dip angle of segment A′B′ is 80° (Figure 10). Assuming the axial surface orientation of 60°, if the hanging wall undergoes a horizontal slip distance of x, the displacement AD in the shallow segment of fault ABC is 0.87x, while the displacement A′D′ in the shallow segment of fault A′B′C′ is 1.35x. Based on the results obtained from the shallow segments, one might conclude that fault A′B′C′ exhibits greater activity than fault ABC. However, this conclusion is erroneous when considering the deep segments.

Furthermore, if one were to infer the regional horizontal extension based on the calculation of horizontal displacement in the shallow segment of the fault, it would result in conclusions that deviate from the actual scenario. The horizontal displacement of AD measures 0.75x, while the horizontal displacement of A′D′ amounts to 0.23x. Based on these values, one might perceive fault ABC to have a greater extension rate compared to fault A′B′C′. However, in reality, both faults exhibit equal extension rates.

When there is deposition of growth strata, previous researches (Huang et al., 2014; Zhang et al., 2020) attempt to estimate the strength of tectonic extension based on the thickness of the growth strata. However, such an approach sometimes is problematic. For fault ABC, the thickness of the growth strata, which is equivalent to the vertical displacement AD, is 0.43x. For fault A′B′C′, the thickness of the growth strata, equivalent to the vertical displacement A′D′, is 1.33x. Based on the thickness of the growth strata, fault A′B′C′ appears to exhibit a stronger tectonic extension than fault ABC. Nevertheless, in reality, the extension rates of these two faults are equal because BE is equal to B′E′.

5.2 Convex fault bend

For a fault with only one convex fault bend, the relationship between the slip rates along the upper segment and the lower segment can be determined based on Eq. 11:

$$\frac{r_1}{r_2} = \frac{\sin(\psi - \theta_2)}{\sin(\psi - \theta_1)} \qquad (46)$$

where r_1 is the slip rate along the upper fault segment, r_2 is the slip rate along the lower segment, ψ is the dip angle of axial surface, θ_1 representing the dip of the upper fault segment, θ_2 representing the dip of the lower fault segment.

Similarly, we take ψ as 60° as an example to investigate the proportional relationship between r_1 and r_2 under different values of θ_1 and θ_2.

Figure 11 depicts the values of r_1/r_2 corresponding to different θ_1 when θ_2 is respectively set at 10°, 20°, 30°, 40°, 50°, and 59°. Unlike concave bends, for convex bends, regardless of the value of θ_2, the ratio r_1/r_2 continuously increases with the increase of θ_1, and its maximum value is limited to 1. This implies that for convex bends, the slip rate along the upper segment of the fault is always smaller than that along the lower segment.

It is noteworthy that when θ_2 approaches the dip angle of axial surface, the value of r_1/r_2 becomes very small (Figures 11, 12A). This implies a significant reduction in the activity of the upper segment of the fault, with a substantial portion of the fault displacement being absorbed by the shear zone. Consequently, this may lead to the transformation of the shear zone into a new fault and cause the cessation of activity in the upper segment of the fault.

When θ_2 equals the dip angle of axial surface, the value of r_1/r_2 becomes 0, and the width of the shear zone also becomes 0 (Figure 12B). This implies the complete cessation of activity in the upper segment of the fault, transforming the shear zone into a new fault.

This model is incapable of predicting scenarios where θ_2 exceeds the dip angle of axial surface since, in such instances, a reverse offset would occur along the upper segment of the fault (Figure 12C). This discrepancy clearly contradicts the extensional characteristics of the deformation. When θ_2 exceeds the dip angle of axial surface, we hypothesize that two potential scenarios could arise. In the first scenario, the hanging wall of the fault undergoes deformation following alternative patterns, whereas in the second scenario, the lower segment of the fault directly propagates upward, inducing a transformation of the formerly convex fault into a planar fault.

6 Conclusion

The study derived relationships between fault slip rates at different depths based on the inclined shear model. The following conclusions were obtained:

(1) For the listric normal fault, if the fault dip angles differ at two different depths, their slip rates generally vary. The extent of variation primarily depends on the fault dip angles at the respective depths, the type of fault bend, and the dips of the axial surfaces.

(2) In the case of a concave fault bend, when the dip of the lower fault segment is between 0° and 30°, the ratio of slip rates between the upper and lower segments initially decreases with an increase in the dip of the upper fault segment. Subsequently, the ratio increases with an increase in the dip of the upper fault segment, but the magnitude of decrease is not as significant as the magnitude of increase. If the dip of the lower fault segment exceeds 30°, the ratio of slip rates between the upper and lower segments continually increases with an increase in the dip of the upper fault segment.

(3) For a convex fault bend, regardless of the dip of the lower fault segment, the ratio of slip rates between the upper and lower segments continually decreases with an increase in the dip of the upper fault segment.

(4) For the listric normal fault, as it tends to be nearly horizontal at greater depths, the slip rate obtained on the shallow fault segment with a large dip angle is generally larger than that at deeper depths, potentially up to twice as large. Conversely, if the shallow fault segment has a small dip angle, the slip rate obtained there is slightly smaller than that at deeper depths.

(5) Based on the dip-slip and horizontal displacement of shallow faults, as well as the thickness of the growth strata, to infer the strength of regional horizontal extension is prone to yielding erroneous conclusions. To achieve a more accurate assessment, a comprehensive analysis integrating the geometric configuration of the fault and deformation pattern of the hanging wall is necessary.

(6) Between 24.6 and 33 Ma, the Chengnan Fault exhibited slip rates of 155–206 m/Ma, which increased to 438–581 m/Ma from 33 to 43.5 Ma, and subsequently remained in the range of 305–404 m/Ma from 43.5 to 65 Ma. The calculation of slip rates for the Chengnan Fault at various depths indicates a decreasing trend from segment A2A3 to segment A4A5, followed by an increasing trend from segment A4A5 to segment A16A17.

Data availability statement

The original contributions presented in the study are included in the article/supplementary material, further inquiries can be directed to the corresponding author.

Author contributions

YZ: Conceptualization, Data curation, Formal Analysis, Funding acquisition, Investigation, Methodology, Project administration, Resources, Software, Supervision, Validation, Visualization, Writing–original draft, Writing–review and editing.

Funding

Acknowledgments

Conflict of interest

The author declares that the research was conducted in the absence of any commercial or financial relationships that could be construed as a potential conflict of interest.

Publisher's note

References

Anderson, J. G., Wesnousky, S. G., and Stirling, M. W. (1996). Earthquake size as a function of fault slip rate. *Bull. Seismol. Soc. Am.* 86, 683–690. doi:10.1785/BSSA0860030683

Benedetti, L., Finkel, R., Papanastassiou, D., King, G., Armijo, R., Ryerson, F., et al. (2002). Post-glacial slip history of the Sparta fault (Greece) determined by 36Cl cosmogenic dating: evidence for non-periodic earthquakes. *Geophys. Res. Lett.* 29, 1246. doi:10.1029/2001GL014510

Blakeslee, M. W., and Kattenhorn, S. A. (2013). Revised earthquake hazard of the Hat Creek fault, northern California: a case example of a normal fault dissecting variable-age basaltic lavas. *Geosphere* 9, 1397–1409. doi:10.1130/GES00910.1

Bull, J. M., Barnes, P. M., Lamarche, G., Sanderson, D. J., Cowie, P. A., Taylor, S. K., et al. (2006). High-resolution record of displacement accumulation on an active normal fault: implications for models of slip accumulation during repeated earthquakes. *J. Struct. Geol.* 28, 1146–1166. doi:10.1016/j.jsg.2006.03.006

Dula, W. F. (1991). Geometric models of listric normal faults and rollover folds. *AAPG Bull.* 75, 1609–1625. doi:10.1306/0C9B29B1-1710-11D7-8645000102C1865D

Friedrich, A. M., Wernicke, B. P., Niemi, N. A., Bennett, R. A., and Davis, J. L. (2003). Comparison of geodetic and geologic data from the Wasatch region, Utah, and implications for the spectral character of Earth deformation at periods of 10 to 10 million years. *J. Geophys. Res. Solid Earth* 108, 2199. doi:10.1029/2001JB000682

Galadini, F., and Galli, P. (2000). Active tectonics in the central Apennines (Italy) - input data for seismic hazard assessment. *Nat. Hazards* 22, 225–270. doi:10.1023/A:1008149531980

Groshong, R. H. (1989). Half-graben structures: balanced models of extensional fault-bend folds. *Geol. Soc. Am. Bull.* 101, 96–105. doi:10.1130/0016-7606(1989)101<0096:HGSBMO>2.3.CO;2

Hauge, T. A., and Gray, G. G. (1996). A critique of techniques for modelling normal-fault and rollover geometries. *Geol. Soc. Lond. Spec. Publ.* 99, 89–97. doi:10.1144/gsl.sp.1996.099.01.08

Huang, L., Liu, C. Y., Wang, Y., Zhao, J., and Mountney, N. P. (2014). Neogene-Quaternary postrift tectonic reactivation of the Bohai Bay Basin, eastern China. *AAPG Bull.* 98, 1377–1400. doi:10.1306/03071413046

Kerr, H. G., and White, N. (1992). Laboratory testing of an automatic method for determining normal fault geometry at depth. *J. Struct. Geol.* 14, 873–885. doi:10.1016/0191-8141(92)90047-Z

Li, S., Zhao, G., Dai, L., Zhou, L., Liu, X., Suo, Y., et al. (2012). Cenozoic faulting of the Bohai Bay Basin and its bearing on the destruction of the eastern north China craton. *J. Asian Earth Sci.* 47, 80–93. doi:10.1016/j.jseaes.2011.06.011

McClymont, A. F., Villamor, P., and Green, A. G. (2009). Fault displacement accumulation and slip rate variability within the Taupo Rift (NewZealand) based on trench and 3-D ground-penetrating radar data. *Tectonics* 28, TC4005. doi:10.1029/2008TC002334

Mitchell, S. G., Matmon, A., Bierman, P. R., Enzel, Y., Caffee, M., and Rizzo, D. (2001). Displacement history of a limestone normal fault scarp, northern Israel, from cosmogenic 36Cl. *J. Geophys. Res. Solid Earth* 106, 4247–4264. doi:10.1029/2000JB900373

Mouslopoulou, V., Walsh, J. J., and Nicol, A. (2009). Fault displacement rates on a range of timescales. *Earth Planet. Sci. Lett.* 278, 186–197. doi:10.1016/j.epsl.2008.11.031

Nicol, A., Walsh, J., Berryman, K., and Villamor, P. (2006). Interdependence of fault displacement rates and paleoearthquakes in an active rift. *Geology* 34, 865–868. doi:10.1130/G22335.1

Nicol, A., Walsh, J., Watterson, J., and Underhill, J. R. (1997). Displacement rates of normal faults. *Nature* 390, 157–159. doi:10.1038/36548

Nicol, A., Walsh, J. J., Manzocchi, T., and Morewood, N. (2005). Displacement rates and average earthquake recurrence intervals on normal faults. *J. Struct. Geol.* 27, 541–551. doi:10.1016/j.jsg.2004.10.009

Nicol, A., Walsh, J. J., Villamor, P., Seebeck, H., and Berryman, K. R. (2010). Normal fault interactions, paleoearthquakes and growth in an active rift. *J. Struct. Geol.* 32, 1101–1113. doi:10.1016/j.jsg.2010.06.018

Qi, J., and Yang, Q. (2010). Cenozoic structural deformation and dynamic processes of the Bohai Bay basin province, China. *Mar. Petroleum Geol.* 27, 757–771. doi:10.1016/j.marpetgeo.2009.08.012

Ren, J. (2004). Tectonic significance of S6' boundary in dongying depression, Bohai gulf basin. *Earth Science-Journal China Univ. Geosciences* 29, 69–82. doi:10.3321/j.issn:1000-2383.2004.01.013

Schlagenhauf, A., Gaudemer, Y., Benedetti, L., Manighetti, I., Palumbo, L., Schimmelpfennig, I., et al. (2010). Using *in situ* Chlorine-36 cosmonuclide to recover past earthquake histories on limestone normal fault scarps: a reappraisal of methodology and interpretations. *Geophys. J. Int.* 182, 36–72. doi:10.1111/j.1365-246X.2010.04622.x

Schlagenhauf, A., Manighetti, I., Benedetti, L., Gaudemer, Y., Finkel, R., Malavieille, J., et al. (2011). Earthquake supercycles in central Italy inferred from 36Cl exposure dating. *Earth Planet. Sci. Lett.* 307, 487–500. doi:10.1016/j.epsl.2011.05.022

White, N. (1992). A method for automatically determining normal fault geometry at depth. *J. Geophys. Res. Solid Earth* 97, 1715–1733. doi:10.1029/91JB02565

White, N., and Yielding, G. (1991). Calculating normal fault geometries at depth: theory and examples. *Geol. Soc. Lond. Spec. Publ.* 56, 251–260. doi:10.1144/gsl.sp.1991.056.01.18

White, N. J., Jackson, J. A., and McKenzie, D. P. (1986). The relationship between the geometry of normal faults and that of the sedimentary layers in their hanging walls. *J. Struct. Geol.* 8, 897–909. doi:10.1016/0191-8141(86)90035-0

Withjack, M. O., Islam, Q. T., and La Pointe, P. R. (1995). Normal faults and their hanging-wall deformation: an experimental study. *AAPG Bull.* 79, 1–17. doi:10.1306/8D2B1494-171E-11D7-8645000102C1865D

Withjack, M. O., and Peterson, E. T. (1993). Prediction of normal-fault geometries—a sensitivity analysis. *AAPG Bull.* 77, 1860–1873. doi:10.1306/BDFF8F60-1718-11D7-8645000102C1865D

Withjack, M. O., and Schlische, R. W. (2006). Geometric and experimental models of extensional fault-bend folds. *Geol. Soc. Lond. Spec. Publ.* 253, 285–305. doi:10.1144/GSL.SP.2006.253.01.15

Xiao, H., and Suppe, J. (1992). Origin of rollover. *AAPG Bull.* 76, 509–529. doi:10.1306/BDFF8858-1718-11D7-8645000102C1865D

Yao, Y., Xu, D., Han, Y., Yin, Z., and Zhang, H. (2007a). Astrostratigraphic age analysis of the eocene–oligocene boundary in the jiyang depression, shandong. *J. Stratigr.* 31, 483–494. doi:10.19839/j.cnki.dcxzz.2007.s2.008

Yao, Y., Xu, D., Zhang, H., Han, Y., Zhang, S., Yin, Z., et al. (2007b). A brief introduction to the Cenozoic astrostratigraphic time scale for the Dongying Sag, Shandong. *J. Stratigr.* 31, 423–429. doi:10.19839/j.cnki.dcxzz.2007.s2.002

Youngs, R. R., and Coppersmith, K. J. (1985). Implications of fault slip rates and earthquake recurrence models to probabilistic seismic hazard estimates. *Bull. Seismol. Soc. Am.* 75, 939–964. doi:10.1785/BSSA0750040939

Zhang, Y., Dilek, Y., Zhang, F. Q., Chen, H. L., Zhu, C. T., and Hao, X. F. (2020). Structural architecture and tectonic evolution of the cenozoic zhanhua sag along the tan-Lu fault zone in the eastern north China: reconciliation of tectonic models on the origin of the Bohai Bay Basin. *Tectonophysics* 775, 228303. doi:10.1016/j.tecto.2019.228303

Zhao, F., Jiang, S., Li, S., Zhang, H., Wang, G., Lei, J., et al. (2016). Cenozoic tectonic migration in the Bohai Bay Basin, east China. *Geol. J.* 51, 188–202. doi:10.1002/gj.2787